



ZnO nanoparticles and biocidal effect of nanostructured ZnO films on *Escherichia coli*

Nabila Bouasla^a, Sihem Abderrahmane^{a,*}, Sameh Athmani^a, Amel Oulabbas^a, Mohamed Bououdina^b

^aLaboratoire d'Ingénierie de Surfaces (L.I.S), University Badji Mokhtar, BP 12, 23000 Annaba, Algeria, Tel. +213670056720; email: abderrahmanesihem@yahoo.fr (S. Abderrahmane), Tel. +213657685029; email: nbouasla@yahoo.fr (N. Bouasla), Tel. +213671203902; email: samehathmani@yahoo.fr (S. Athmani), Tel. +213668152031; email: ameloulabbas@hotmail.com (A. Oulabbas)

^bDepartment of Physics, College of Science, University of Bahrain, PO Box 32038, Bahrain, Tel. +97317437585; email: mboudina@gmail.com

Received 9 May 2017; Accepted 20 January 2018

ABSTRACT

The biocidal effect of ZnO nanostructured films was studied using *Escherichia coli* ATCC 43897. The ZnO nanoparticles were synthesized in diethylene glycol by using zinc acetate forced hydrolysis. X-ray diffraction analysis confirmed the formation of single wurtzite-type ZnO phase with a crystallite size of 20.59 nm. Transmission electron microscopy observations revealed spherical-shaped particles in the nanoscale regime with a mean particle size of 21.96 nm. It was found that the addition of trioctylphosphine during synthesis favored much improved dispersion of ZnO nanoparticles, with smaller particle size; that is, 16.28 nm. Meanwhile, ZnO film grown onto glass substrate by spin-coating revealed single phase with the formation of aggregates (≈ 700) having mushroom-like morphology formed of very fine particles in the nanoscale regime. The as-deposited nanostructured films exhibited a hydrophilic character. The classical bacteriological and electrochemical impedance spectroscopy measurements enabled the biocidal effect of ZnO nanostructured films with 94% inactivation efficiency after 90 min of contact time.

Keywords: ZnO; Spin-coating; Nanostructured film; Biocide effect; *E. coli*; EIS

1. Introduction

Zinc oxide (ZnO) is a semiconductor with unique and excellent properties [1,2]. Recently, it attracted considerable attention in the photocatalytic activity of environmental pollutants, due to its direct band gap [3] and its high efficiency in the photodegradation of various organic dyes such as thionine, methylene blue, acridine orange, benzene and its derivatives [4–8]. It is important to highlight that ZnO has been extensively studied among other oxides because of its high photocatalytic efficiency, low cost and non-toxicity [9,10]. In addition, it offers various

applications in optoelectronic [11], piezoelectric and electronic [12] devices.

ZnO can be prepared in the form of thin films and nanoparticles (NPs). The latter can be used in various applications such as sunscreens products, chemical sensors, solar cells [13] and medicine [14]. Recent researches have shown that ZnO NPs have an antibacterial activity against *E. coli* bacteria [15–18]. Therefore, they have been proposed for the preservation of agricultural and food products. ZnO NPs obtained by an ecological method show a high photocatalytic activity for the degradation of 2-phenylbenzimidazole-5-sulfonic acid [19]. It was found that ZnO NPs are more catalytically active for the photodegradation of methyl orange under simulated sunlight than commercial ZnO [20]. It is worth

* Corresponding author.

noting that the morphology of ZnO NPs has an influence on photocatalytic activity [21,22]. rGO/ZnO nanohybrids (rGO: reduced graphene) prepared by a rapid microwave-assisted process exhibited powerful photocatalytic activity for the decolorization of rhodamine-B and methylene blue dyes under visible-light illumination [23]. Moreover, Zhou et al. [24] showed that uniform hamburger-like mesoporous carbon-incorporated ZnO (MC-ZnO) nanoarchitectures prepared by a simple solvothermal method demonstrated photocatalytic activity for the decolorization of photosensitized dyes (congo red and rhodamine-B) under visible-light illumination.

Moreover, nanostructured ZnO films can be deposited onto a variety of substrates such as silicon, glass and indium tin oxide [25], using numerous methods such as sol-gel [26,27], spin-coating [28,29], sol-gel spin-coating [30,31], spin-coating pyrolysis [32], pulsed laser deposition [33], hydrothermal [25,34] and spray method [35].

In this regards, it is important to mention that the adopted synthesis/deposition approach for NPs/films has tremendous effects on phase stability and purity, shape and size of particles/grains, agglomeration (dispersion), stoichiometry (formation of point defects (such as oxygen vacancies), as well as surface topography and roughness. Therefore, NPs/films properties can be tuned accordingly.

On the other side, the antibacterial activities against the *Escherichia coli* bacterium of nanostructured ZnO films obtained by sol-gel dip-coating [36] and by ultrasonic irradiation [37] methods were proven.

In this study, ZnO NPs were successfully synthesized by polyol method, and then deposited onto glass substrate by cost-effective spin-coating method. The bactericidal effect of nanostructured ZnO film against the *E. coli* bacterium was investigated by the classical bacteriological method and as novelty obtaining an impedancemetric response using a transient electrochemical method; that is electrochemical impedance spectroscopy (EIS).

2. Materials and methods

2.1. Synthesis of ZnO nanoparticles

For the synthesis of ZnO NPs, zinc acetate forced hydrolysis is carried out in diethylene glycol (DEG; Sigma-Aldrich) [16]. To do that, we added zinc acetate in 80 mL of DEG and 1 mL of water. The hydrolysis ratio is:

$$H = \frac{n_{\text{H}_2\text{O}}}{n_{\text{Zn}^{2+}}} = 7.62 \quad (1)$$

In order to obtain monodispersed ZnO NPs, 0.3 mL of trioctylphosphine (TOP) was added to the reaction medium, followed by stirring at a temperature of 180°C for 1 h time.

2.2. Preparation of nanostructured ZnO films

For nanostructured ZnO film preparation, 200 mg of ZnO NP dried powder was mixed with 25 mL of ethanol-2-methoxy in a beaker immersed in an ultrasonic bath. The obtained solution was then deposited onto a glass substrate. The latter

was precleaned before deposition in concentrated nitric acid for 30 min, then washed with distilled water and finally with acetone for 30 min before vacuum drying. A 300 μL of the solution was dripped with a micropipette onto glass substrate and then spread using a spinner (DOLOS) ESC (cTagLaSDIN 1949) at 2,500 rpm during 40 s.

2.3. Nanoparticles and nanostructured films characterizations

The crystal structure and phase purity of the as-prepared ZnO NPs and thin films were characterized by X-ray diffraction (XRD) using PRO PANalytical diffractometer equipped with Co $K\alpha$ radiation source (wavelength $\lambda = 1.78 \text{ \AA}$). Morphological (shape and size) observations were carried out by transmission electron microscopy (TEM) using Jeol-100 microscope operating at 100 kV. The particle size was obtained from TEM images recorded using a digital camera and the SAISAM (Microvision Instruments) software, calculating the mean diameter of the surface by a statistical analysis carried out by counting about 100 particles considered as spherical. Surface observations of ZnO thin film were performed by scanning electron microscopy (SEM) using Zeiss supra 40 operating at 2.5 kV and measured the contact angle with water.

2.4. Preparation of bacterial solution

The bacterial strain used in this work is *E. coli* (ATCC 43897) obtained from the University of Bingol-Turkey, Bacteriology Laboratory. To prepare the bacterial solution, *E. coli* is seeded in the liquid medium (Mueller Hinton Broth) then incubated at 37°C with continuous stirring for 18 h and finally centrifuged for 10 min at 4,500 rpm. Physiological water is added to the obtained pellet in order to obtain a cellular solution. The latter is diluted with sterilized distilled water up to 0.5 optic density corresponding to 4×10^8 colony forming units (CFU)/mL (stock solution) using a JENWAY6405UV/VIS spectrophotometer.

2.5. Study of biocidal effect

To study the biocidal effect of ZnO nanostructured films on *E. coli*, a glass substrate of 2.5 cm^2 , was placed in a beaker containing 150 mL of phosphate buffer saline (PBS) solution and 300 μL of diluted stock solution at 10^{-1} . The resultant solution was then incubated at 37°C for 2 h under continuous stirring. Each 30 min, 25 μL of solution was collected and seeded into Petri dishes containing nutrient plate count agar, then placed in an incubator at 37°C for 48 h. Finally, the bacteriological enumeration was performed.

However, to highlight the nanostructured ZnO film biocidal efficiency, a comparison between the obtained colonies number with control experiment has been carried out using the same bacterial solution onto glass substrate without nanostructured film.

2.6. Electrochemical impedance spectroscopy measurements

The experimental device used to study the nanostructured ZnO film current response consisted of potentiostat/galvanostat/ZRA type Gamry Interface 1000 with Gamry

Framework software. This device was linked to a microcomputer and connected to an electrochemical cell with three electrodes: (i) nanostructured ZnO film onto a 2.5 cm² glass substrate as working electrode; (ii) saturated calomel as reference electrode; and (iii) platinum (Pt) wire as auxiliary electrode. The electrolyte was the bacterial solution consisting of 150 mL PBS and 300 μL diluted stock solution at 10⁻¹ and incubated at 37°C during 30 min, in which the working electrode is immersed.

3. Results and discussion

3.1. Characterization of NPs and nanostructured films

Fig. 1 displays XRD patterns of ZnO and ZnO-TOP NPs. For both samples, well-defined and broad diffraction peaks are observed at 37.05°, 40.18°, 42.34°, 55.78°, 66.78°, 74.51°, 78.85°, 80.89°, and 82.33°, corresponding to (100), (002), (101), (102), (110), (103), (200), (112), and (201) reflections, respectively, of the hexagonal (space group *P6₃mmc*) structure of ZnO wurtzite, in agreement with JCPDS card No. 80-0075. No additional peaks can be detected, indicating the formation of pure and single ZnO phase. The peaks intensity is relatively high, indicating high quality and good crystallinity. However, it can be observed that ZnO peaks are comparatively more intense compared with ZnO-TOP, due to TOP. In addition, the relatively large reflections width is mainly associated with small grain size and low internal stress contribution induced by severe mechanical deformation [38].

The mean crystallite size (*D*) of ZnO and ZnO-TOP samples is estimated using the Debye–Scherer equation [39,40]:

$$D = \frac{0.9\lambda}{\beta_{hkl} \cos\theta} \quad (2)$$

where λ is X-rays' wavelength ($\lambda = 1.78 \text{ \AA}$); θ is the Bragg diffraction angle of the reflection; and β_{hkl} represents the full width at half maximum (FWHM) of the corresponding reflection.

The instrumental broadening (β_{hkl}) corresponding to each diffraction peak of ZnO NPs was corrected using Eq. (3):

$$\beta_{hkl} = [(\beta_{hkl})_{\text{Measured}} - (\beta_{hkl})_{\text{Instrumental}}] \quad (3)$$

From Table 1, the mean crystallite size of ZnO and ZnO-TOP is found to be 20.59 and 16.57 nm, respectively. The decrease in ZnO-TOP crystallite size can be attributed to the addition of TOP agent, playing a double role; grain growth inhibitor and favoring better dispersion of NPs.

The interplanar spacing d_{hkl} and the lattice constants (*a* and *c*) of ZnO and ZnO-TOP NPs with the hexagonal wurtzite structure are calculated from the lattice geometry equation as indicated below [39,40]:

$$\lambda = 2 \sin\theta \quad (4)$$

$$\frac{1}{d^2} = \frac{4}{3} \cdot \frac{(h^2 + hk + k^2)}{a^2} + \frac{l^2}{c^2} \quad (5)$$

The lattice constants *a* and *c* can be calculated from (100) and (002) reflections, respectively.

The unit cell volume (*V*) of a hexagonal system can be calculated from the following equation [41]:

$$V = 0.866 \times a^2 \times c \quad (6)$$

The calculated lattice constants and the corresponding unit cell volume are given in Table 2. It can be observed that the values of the lattice parameters for both ZnO and ZnO-TOP are slightly smaller compared with the standard values obtained for bulk ZnO, indicating the presence of some constraints. The lattice stress can result in the displacement

Table 1
XRD data of ZnO and ZnO-TOP NPs

Samples	2θ (°)	(hkl)	<i>d</i> (Å)	FWHM (rad)	Crystallite size (nm)
ZnO	37.05	(100)	2.8031	0.0088	19.33
	40.18	(002)	2.5812	0.0068	25.30
	42.35	(101)	2.4688	0.0090	19.14
	55.78	(102)	1.9037	0.0113	16.11
	66.78	(110)	1.6182	0.0105	18.27
	74.52	(103)	1.4711	0.0104	19.37
	78.86	(200)	1.4016	0.0081	25.74
	80.90	(112)	1.3798	0.0098	21.50
	82.33	(201)	1.3588	0.0140	15.32
ZnO-TOP	37.11	(100)	2.79874	0.0114	20.59
	40.23	(002)	2.59097	0.0094	18.13
	42.40	(101)	2.46196	0.0112	15.35
	55.86	(102)	1.90170	0.0113	16.15
	66.82	(110)	1.61671	0.0129	14.96
	74.55	(103)	1.46985	0.0137	14.74
	79.02	(200)	1.39937	0.0081	23.96
	80.94	(112)	1.37134	0.0147	14.40
	82.33	(201)	1.35877	0.0103	20.85

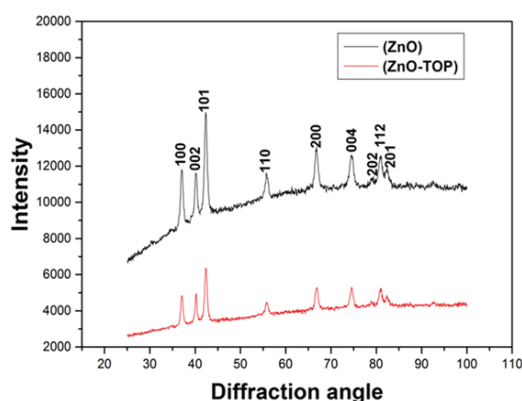


Fig. 1. XRD patterns of ZnO and ZnO-TOP nanoparticles.

of atoms within the unit cell with respect to their normal positions as well as other factors such as dislocation, surface restructuring, vacancies, and interstitials [42].

In order to estimate the amount of strain present within ZnO and ZnO-TOP NPs, the well-known Williamson–Hall method (W-H) has been used, where the observed XRD line broadening due to crystallite size and the contribution of strain, can be written as follows [43]:

$$\beta_{hkl} = \beta_t + \beta_e \quad (7)$$

where β_t is the crystallite size broadening; β_e is the strain-induced broadening; and β_{hkl} is the FWHM of instrumental corrected broadening.

The diffraction line broadening due to the imperfection and distortion of the crystals is given by:

$$\beta_e = 4\varepsilon \tan \theta_{hkl} \quad (8)$$

where ε root mean square represents the value of the microstrain.

The diffraction line broadening due to the crystallite size can be obtained from the Debye–Scherer formula.

Considering the contribution of these two line broadenings, Eq. (7) can be written as follows [43,44]:

$$\beta_{hkl} \cos \theta = \frac{K\lambda}{D} + 4\varepsilon \sin \theta \quad (9)$$

Eq. (9) represents the uniform deformation model (UDM), where all properties of the material are independent of the direction in which they were measured.

By plotting the graph of $\beta_{hkl} \cos \theta$ vs. $4 \sin \theta$ for ZnO (Fig. 2(a)) and ZnO-TOP (Fig. 2(b)), the strain (ε) represents the slope of the fitting line while the crystallite size (D) can be determined from the intersection with the vertical axis [45].

According to Fig. 2(a), a positive slope (0.0022) is observed, which can be due to the presence of tensile strain attributed to the lattice distortion [44], while a decrease in the lattice parameters is observed. From Fig. 2(b), the negative slope (–0.0051) indicates the presence of compressive strain may be due to lattice contraction [42]. This is in good agreements with the calculated lattice constants reported in Table 2.

Table 3 summarizes the geometric parameters of ZnO NPs obtained from Scherrer formula, W-H analysis and TEM results.

The mean crystallite size values obtained from UDM are found to be consistent with those obtained from the Scherrer formula and TEM. Herein, it is important to highlight the difference between the crystallite size calculated from XRD and the particle size estimated from TEM images; a particle is made of several crystallites. Since both values are close, this means that the as-prepared NPs are in fact made of one crystallite (crystal).

Since the calculation of crystallites size using Scherrer's formula not accurate, TEM analysis was performed in order to confirm the size of ZnO NPs. Fig. 3(a) shows that ZnO NPs are almost spherical with a mean size of 21.96 nm, while Fig. 3(b) for ZnO-TOP presents well dispersed ZnO

Table 2

Lattice parameters and unit cell volume of ZnO and ZnO-TOP NPs

Samples	Lattice parameters (Å)		c/a ratio	Volume (Å) ³
	a = b	c		
ZnO	3.236	5.161	1.597	46.80
ZnO-TOP	3.226	5.179	1.605	46.68
JCPDS N°. 80-0075	3.253	5.206	1.603	47.77

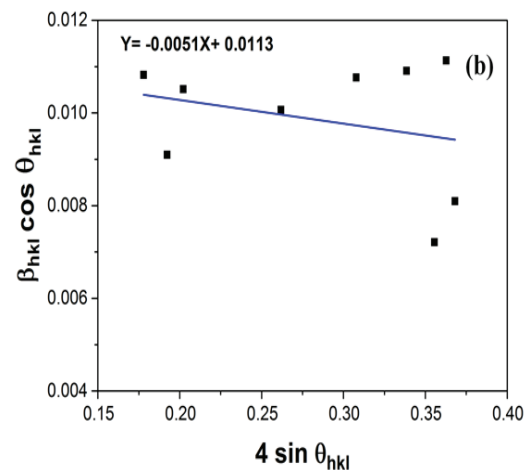
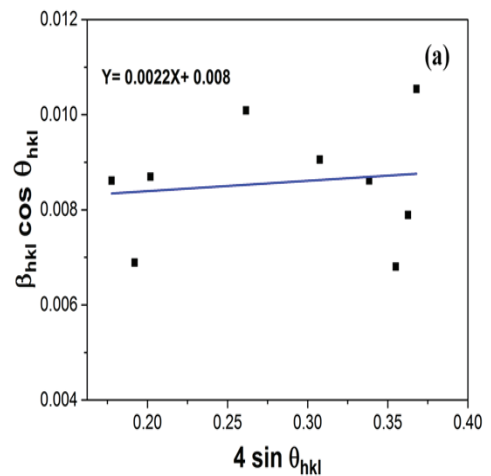


Fig. 2. W-H analysis of (a) ZnO and (b) ZnO-TOP NPs assuming UDM.

Table 3

Geometric parameters of ZnO and ZnO-TOP NPs

Samples	Debye–Scherer formula D (nm)	(W-H method) UDM		Particle size from TEM (nm)
		D (nm)	$\varepsilon \times 10^{-3}$	
ZnO	20.59	12.57	2.2	21.96
ZnO-TOP	16.57	8.85	5.5	16.28

NPs having a smaller mean size of 16.28 nm. It is clear from the histogram of grain size distribution that the particle size varies in relatively narrow range of 15–35 nm for ZnO (Fig. 3(c)) whereas for ZnO-TOP (Fig. 3(d)) in the range 5–25 nm. For ZnO and ZnO-TOP, around 59% and 78% of particles have an average size of the order 21.96 and 16.28 nm, respectively, indicating an additional positive effect of using TOP agent. In addition, these particles have approximately the average crystallite size determined by XRD. From the above results, it can be concluded that TOP is a good dispersing agent.

Fig. 4 displays SEM micrograph of nanostructured ZnO film prepared by spin-coating method. It can be observed the formation of aggregates with various micrometric size (≈ 700 nm) having mushroom-like morphology and covering the entire surface of glass substrate. The ZnO film exhibits high porosity and important roughness. However, a zoom of a selected aggregate indicates that it is formed by very fine particles in the nanoscale regime. This kind of morphology is very important for photocatalysis, as it possesses numerous active sites.

Fig. 5 shows the contact angle of water on nanostructured ZnO film. This angle is around 38.14° , which indicates that this film has a hydrophilic character.

3.2. Bactericidal effect of ZnO nanostructured film on *E. coli*

The ZnO nanostructured film bactericidal effect was tested on *E. coli* bacterium. The live bacteria were counted by counting the number of CFU/mL. Fig. 6 shows the evolution of bacteria number vs. contact time. It can be noticed

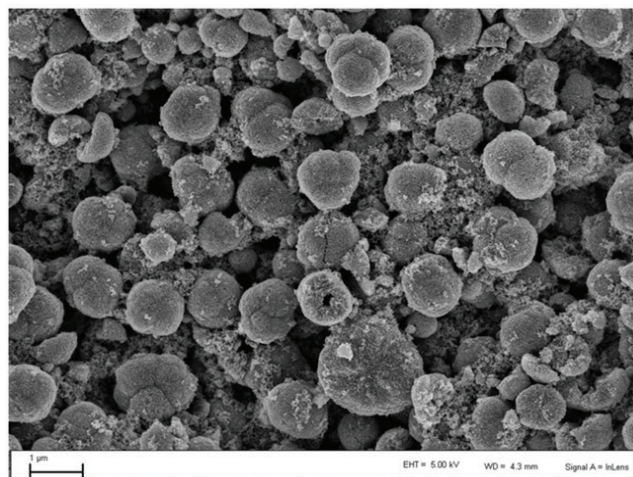


Fig. 4. SEM micrograph of ZnO nanostructured film.

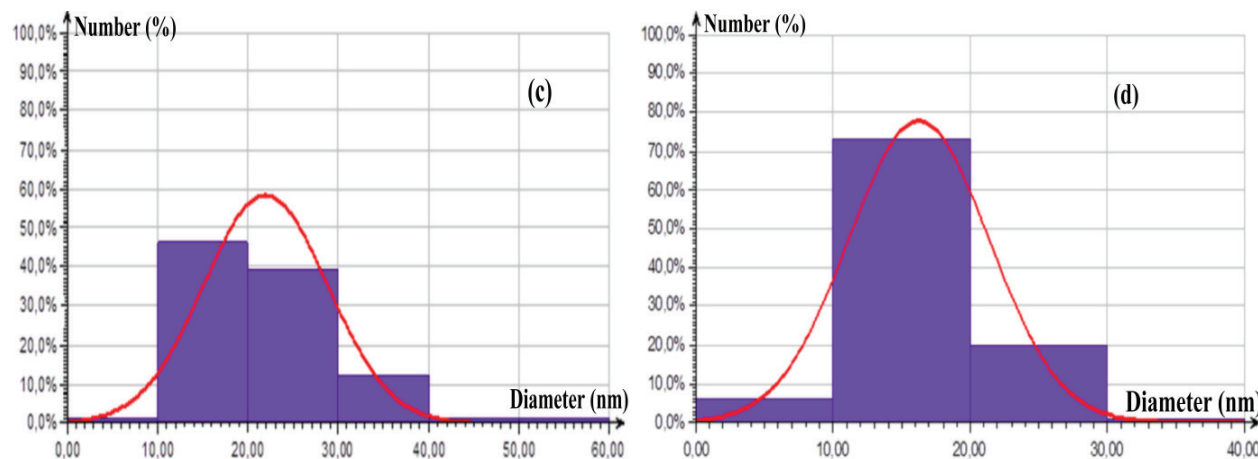
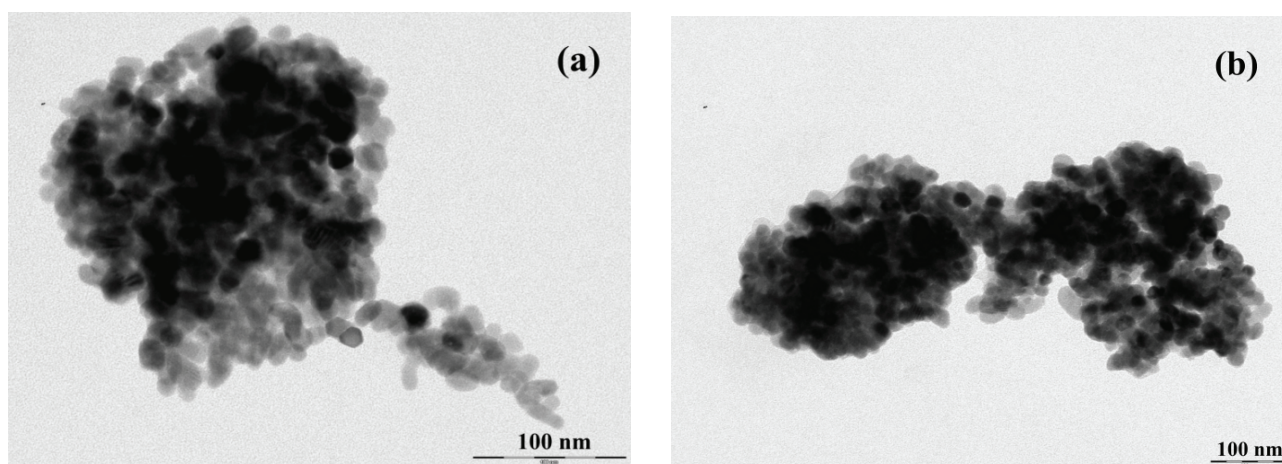


Fig. 3. TEM micrographs of (a) ZnO, (b) ZnO-TOP NPs and the corresponding histograms of size distribution for (c) ZnO, (d) ZnO-TOP.

that after 30 min of contact time, a decrease of 72% of bacteria number is achieved when using nanostructured ZnO film. Further decrease in bacterial number is reached for longer contact time; 94% inactivation is achieved after 90 min. While, without nanostructured ZnO film, the bacteria number remains stable for even longer contact time of 120 min. This result clearly demonstrates the bactericidal effect of the as-grown nanostructured ZnO film on *E. coli*.

Various mechanisms explaining the biocidal action of nanostructured ZnO films on *E. coli* have been reported in the literature; the main are highlighted as follows:

- The interaction of ZnO NPs with bacterial cell induces some modifications of the membrane. This causes an expulsion of the intracellular components and finally the inactivation of the cell [46,47].
- The formation of Zn^{2+} ions and reactive oxygen species (ROS) such as $\bullet OH$ or $\bullet O_2^-$ generated by ZnO NPs, results in the damage of the bacterial cell [46–48].
- In this study, the inactivation of *E. coli* can be explained by the destruction of its cell wall's due to the ROS generated by the nanostructured ZnO film. This has been confirmed by Applerot et al. [49]; the authors proved that the hydroxyl radicals mainly and some species of oxy radicals present in the solution are the major components responsible for the bactericidal effect of ZnO NPs. These ROS were detected in electron spin resonance study.



Fig. 5. Contact angle of water on ZnO nanostructured film.

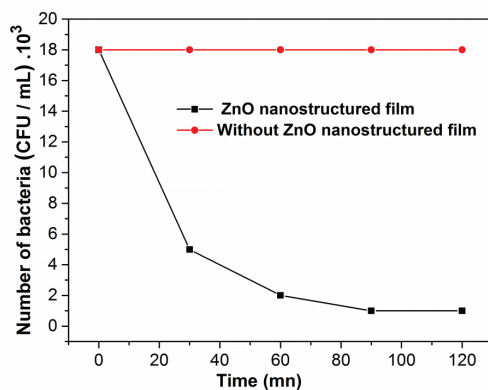


Fig. 6. Variation in bacteria number as a function of contact time.

3.3. Electrochemical impedance diagrams of nanostructured ZnO film without and with *E. coli* bacteria

A study of ZnO film behavior adhered onto a glass substrate and immersed in PBS under hydrostatic conditions was carried out by electrochemical impedancemetry in order to demonstrate the ZnO film biocidal effect on *E. coli* bacteria. The impedance diagrams allow to decompose the reaction mechanisms into elementary processes. The charge transfer phenomena, species adsorption, and diffusion can be evidenced as well as the possibility to determine the characteristic parameters related to each of these processes. A scan of the frequency was performed from high frequencies (HF; 100 kHz) to low frequencies (LF; 10 mHz) with a sinusoidal disturbance of 5 mV amplitude around the free potential. Over this potential range, the system is quasi-stationary [50].

The electrochemical impedance measurements were carried out under similar conditions without and with *E. coli* in the PBS.

The used electrolyte is rich in chloride ions (8 g/L) having a fast electrochemical kinetics. This induces the appearance and growth of the corrosion products that can in fact act as corrosion inhibitors by limiting the oxygen reduction. The modelling of these systems is therefore not easy and must take into account the surface oxidation–reduction reactions.

The aspect of the obtained electrochemical impedance diagram (Fig. 7) shows the existence of a straight line to HF, this may be due to a parasitic or extra process occurring at the electrochemical interface. This phenomenon is probably caused by the use of a saturated calomel reference electrode whose extremity is composed of sintered glass wall [51]. Meanwhile, on the LF range, it is observed that the appearance of an inductive loop perhaps due to a variation in the surface coverage rate induced by adsorption or desorption reactions.

On the other hand, for the Nyquist electrochemical impedance diagram of nanostructured ZnO film into PBS with *E. coli*, obtained after 30 min of immersion time (Fig. 8), a capacitive loop is observed with a large diameter, reflecting a charge transfer resistance, thereby suggests the presence of a resistant passive biofilm at the working electrode surface. This was followed by a second inductive loop, may be caused from the induced biofilm detachment by desorption reactions, which was confirmed the decrease in the bacteria number in the electrolyte.

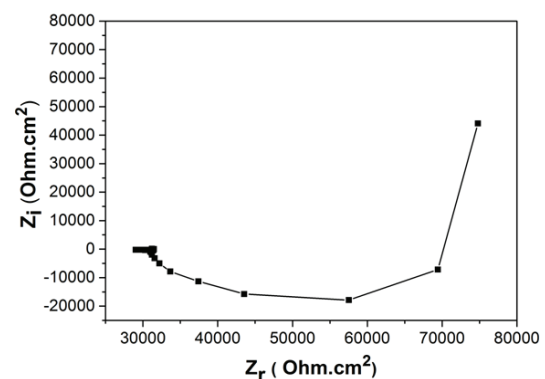


Fig. 7. Electrochemical impedance diagram in Nyquist representation of nanostructured ZnO film into PBS without *E. coli*.

An electrochemical interface can be simulated by an electrical circuit with passive elements such as resistance, capacitance, and inductance. Therefore, an attempt to find out an equivalent circuit to the studied electrochemical system has been carried out. Figs. 9 and 10 represent the equivalent circuits corresponding to the impedance diagram of nanostructured ZnO film into PBS without and with *E. coli*, respectively. An adjustment with the equivalent circuits gave the electrochemical parameters as shown in Table 4.

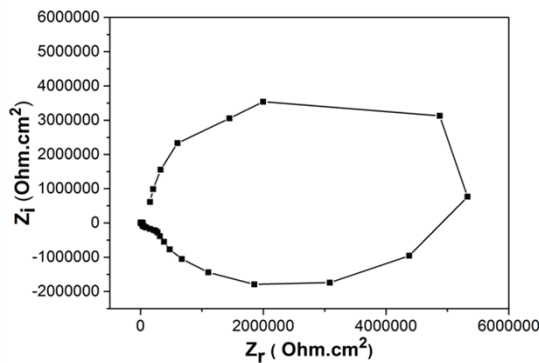


Fig. 8. Electrochemical impedance diagram in Nyquist representation of nanostructured ZnO film into PBS with *E. coli*, after 30 min immersion time.

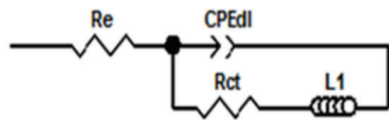


Fig. 9. Equivalent circuit of nanostructured ZnO film immersed in PBS without *E. coli*.

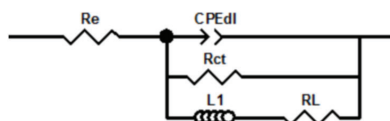


Fig. 10. Equivalent circuit of nanostructured ZnO film immersed in PBS with *E. coli*.

Table 4
Electrochemical parameters deduced from the equivalent circuits of nanostructured ZnO film into PBS without and with *E. coli*

	Without <i>E. coli</i>	With <i>E. coli</i>
R_e (Ω)	31,079	241,650
CPE_{dl} ($pF.s^{1/n}$)	–	3.14
a	–	0.9
R_{ct} ($M\Omega$)	0.03	5
R_L (Ω)	–	41,732
L_1 (H)	0.02	543

4. Conclusion

In this study, ZnO NPs have been synthesized by forced hydrolysis reaction of Zn^{2+} ionic salts followed by the deposition of nanostructured ZnO film onto glass substrate by spin-coating method. XRD analysis confirms the formation of single wurtzite phase with a mean crystallite size of 21.96 nm, which reduces to 16.28 nm when adding TOP as dispersing agent. During film deposition, the NPs form micrometric mushroom-like aggregates with high porosity. This film reveals hydrophilic character. The as-grown nanostructured ZnO film has shown a marked biocidal effect on *E. coli* bacteria, with a 94% inactivation efficiency. This has been confirmed by the classical bacteriological and by the EIS methods. This study demonstrates that the proposed approach by using TOP during synthesis has proved to be very beneficial for controlling the size of NPs with better dispersivity, thereby can be adopted for the preparation of other oxides with improved properties.

Symbols

- H – Hydrolysis ratio
- n – Number of moles, mol
- D – Average crystallite size, nm
- λ – X-rays' wavelength, Å
- θ – Maximum of the Bragg diffraction peak, radian
- β_{hkl} – Full width at half maximum (FWHM) of DRX peak
- d_{hkl} – Interplanar spacing, Å
- a – Cell parameter, Å
- c – Cell parameter, Å
- (h,k,l) – Miller indices
- V – Volume, Å³
- β_t – Crystallite size broadening
- β_c – Strain-induced broadening
- ε – Root mean square value of the microstrain

References

- [1] H. Wang, C. Xie, W. Zhang, S. Cai, Z. Yang, Y. Gui, Comparison of dye degradation efficiency using ZnO powders with various size scales, *J. Hazard. Mater.*, 141 (2007) 645–652.
- [2] N. Padmavathy, R. Vijayaraghavan, Enhanced bioactivity of ZnO nanoparticles—an antimicrobial study, *Sci. Technol. Adv. Mater.*, 9 (2008) 0354004.
- [3] S. Sakthivel, B. Neppolian, M.V. Shankar, B. Arabindoo, M. Palanichamy, V. Murugesan, Solar photocatalytic degradation of azo dye: comparison of photocatalytic efficiency of ZnO and TiO₂, *Sol. Energy Mater. Sol. Cells*, 77 (2003) 65–82.
- [4] S. Anandan, A. Vinu, T. Mori, N. Gokulakrishnan, P. Srinivasu, V. Murugesan, K. Ariga, Photocatalytic degradation of 2,4,6-trichlorophenol using lanthanum doped ZnO in aqueous suspension, *Catal. Commun.*, 8 (2007) 1377–1382.
- [5] H. Fan, X. Zhao, J. Yang, X. Shan, L. Yang, Y. Zhang, X. Li, M. Gao, ZnO-graphene composite for photocatalytic degradation of methylene blue dye, *Catal. Commun.*, 29 (2012) 29–34.
- [6] B. Pare, S.B. Jonnalagadda, H. Tomar, P. Singh, V.W. Bhagwat, ZnO assisted photocatalytic degradation of acridine orange in aqueous solution using visible irradiation, *Desalination*, 232 (2008) 80–90.
- [7] R.Y. Hong, J.H. Li, L.L. Chen, D.Q. Liu, H.Z. Li, Y. Zheng, J. Ding, Synthesis, surface modification and photocatalytic property of ZnO nanoparticles, *Powder Technol.*, 199 (2009) 426–432.
- [8] S.A. Khayyat, M.S. Akhtar, A. Umar, ZnO nanocapsules for photocatalytic degradation of thionine, *Mater. Lett.*, 81 (2012) 239–241.

- [9] J. Liqiang, S. Xiaojun, S. Jing, C. Weimin, X. Zili, D. Yaoguo, F. Honggang, Review of surface photovoltage spectra of nano-sized semiconductor and its applications in heterogeneous photocatalysis, *Sol. Energy Mater. Sol. Cells*, 79 (2003) 133–151.
- [10] Y. Hu, H. Qian, Y. Liu, G. Du, F. Zhang, L. Wang, X. Hu, A microwave-assisted rapid route to synthesize ZnO/ZnS core-shell nanostructures via controllable surface sulfidation of ZnO nanorods, *Cryst. Eng. Commun.*, 13 (2011) 3438–3443.
- [11] W. Lee, M.C. Jeong, J.M. Myoung, Catalyst-free growth of ZnO nanowires by metal-organic chemical vapour deposition (MOCVD) and thermal evaporation, *Acta Mater.*, 52 (2004) 3949–3957.
- [12] K.J. Chen, F.Y. Hung, S.J. Chang, S.J. Young, Z.S. Hu, Effects of crystallization on the optical properties of ZnO nano-pillar thin films by sol-gel method, *Curr. Appl. Phys.*, 11 (2011) 1243–1248.
- [13] Y. Ju-Nam, J.R. Lead, Manufactured nanoparticles: an overview of their chemistry, interactions and potential environmental implications, *Sci. Total Environ.*, 400 (2008) 396–414.
- [14] J. Zhou, N. Xu, Z.L. Wang, Dissolving behavior and stability of ZnO wires in biofluids: a study on biodegradability and biocompatibility of ZnO nanostructures, *Adv. Mater.*, 18 (2006) 2432–2435.
- [15] H. Masoumbaigi, A. Rezaee, H. Hosseini, S. Hashemi, Water disinfection by zinc oxide nanoparticle prepared with solution combustion method, *Desal. Wat. Treat.*, 56 (2015) 2376–2381.
- [16] R. Brayner, R. Ferrari-Iliou, N. Brivois, S. Djediat, M.F. Benedetti, F. Fiévet, Toxicological impact studies based on *Escherichia coli* bacteria in ultrafine ZnO nanoparticles colloidal medium, *Nano Lett.*, 6 (2006) 866–870.
- [17] R. Brayner, The toxicological impact of nanoparticles, *Nano Today*, 3 (2008) 48–55.
- [18] Y. Liu, L. He, A. Mustapha, H. Li, Z.Q. Hu, M. Lin, Antibacterial activities of zinc oxide nanoparticles against *Escherichia coli* 0157:H7, *J. Appl. Microbiol.*, 107 (2009) 1193–1201.
- [19] L. Soto-Vázquez, M. Cotto, C. Morant, J. Duconge, F. Márquez, Facile synthesis of ZnO nanoparticles and its photocatalytic activity in the degradation of 2-phenylbenzimidazole-5-sulfonic acid, *J. Photochem. Photobiol., A*, 332 (2017) 331–336.
- [20] C. Gomez-Solis, J.C. Ballesteros, L.M. Torres-Martínez, I. Juárez-Ramírez, L.A.D. Torres, M.E. Zarazua-Morin, S.W. Lee, Rapid synthesis of ZnO nano-corn-cobs from Nital solution and its application in the photodegradation of methyl orange, *J. Photochem. Photobiol., A*, 298 (2014) 49–54.
- [21] N. Talebian, S.M. Amininezhad, M. Doudi, Controllable synthesis of ZnO nanoparticles and their morphology-dependent antibacterial and optical properties, *J. Photochem. Photobiol., B*, 120 (2013) 66–73.
- [22] C.W. Tang, Study of photocatalytic degradation of methyl orange on different morphologies of ZnO catalysts, *Mod. Res. Catal.*, 2 (2013) 19–24.
- [23] Y. Liu, Y. Hu, M. Zhou, H. Qian, X. Hu, Microwave-assisted non-aqueous route to deposit well-dispersed ZnO nanocrystals on reduced graphene oxide sheets with improved photoactivity for the decolorization of dyes under visible light, *Appl. Catal., B*, 125 (2012) 425–431.
- [24] M. Zhou, X. Gao, Y. Hu, J. Chen, X. Hu, Uniform hamburger-like mesoporous carbon-incorporated ZnO nanoarchitectures: one-pot solvothermal synthesis, high adsorption and visible-light photocatalytic decolorization of dyes, *Appl. Catal., B*, 138 (2013) 1–8.
- [25] N. Ekthammathat, S. Thongtem, T. Thongtem, A. Phuruangrat, Characterization and antibacterial activity of nanostructured ZnO thin films synthesized through a hydrothermal method, *Powder Technol.*, 254 (2014) 199–205.
- [26] L. Znaidi, Sol-gel-deposited ZnO thin films: a review, *Mater. Sci. Eng., B*, 174 (2010) 18–30.
- [27] Y. Liu, L. Yu, Y. Hu, C. Guo, F. Zhang, X.W.D. Lou, A magnetically separable photocatalyst based on nest-like γ -Fe₂O₃/ZnO double-shelled hollow structures with enhanced photocatalytic activity, *Nanoscale*, 4 (2012) 183–187.
- [28] M. Berber, V. Bultó, R. Klöß, H. Hahn, Transparent nanocrystalline ZnO films prepared by spin coating, *Scr. Mater.*, 53 (2005) 547–551.
- [29] H. Çolak, E. Karaköse, Green synthesis and characterization of nanostructured ZnO thin films using *Citrus aurantifolia* (lemon) peel extract by spin-coating method, *J. Alloys Compd.*, 690 (2017) 658–662.
- [30] Y. Natsume, H. Sakata, Zinc oxide films prepared by sol-gel spin-coating, *Thin Solid Films*, 372 (2000) 30–36.
- [31] E. Heredia, C. Bojorge, J. Casanova, H. Cánepa, A. Craievich, G. Kellermann, Nanostructured ZnO thin films prepared by sol-gel spin-coating, *Appl. Surf. Sci.*, 317 (2014) 19–25.
- [32] T. Sahoo, M. Kim, M.H. Lee, L.W. Jang, J.W. Jeon, J.S. Kwak, I.Y. Ko, I.H. Lee, Nanocrystalline ZnO thin films by spin coating-pyrolysis method, *J. Alloys Compd.*, 491 (2010) 308–313.
- [33] R. Vinodkumar, I. Navas, K. Porsezian, V. Ganesan, N.V. Unnikrishnan, V.P. Mahadevan Pillai, Structural, spectroscopic and electrical studies of nanostructured porous ZnO thin films prepared by pulsed laser deposition, *Spectrochim. Acta, Part A*, 118 (2014) 724–732.
- [34] Y. Wang, J. Ning, E. Hu, C. Zheng, Y. Zhong, Y. Hu, Direct coating ZnO nanocrystals onto 1D Fe₃O₄/C composite microtubules as highly efficient and reusable photocatalysts for water treatment, *J. Alloys Compd.*, 637 (2015) 301–307.
- [35] A. Mortezaali, O. Taheri, Z.S. Hosseini, Thickness effect of nanostructured ZnO thin films prepared by spray method on structural, morphological and optical properties, *Microelectron. Eng.*, 151 (2016) 19–23.
- [36] K. Thongsuriwong, P. Amornpitoksuk, S. Suwanboon, Structure, morphology, photocatalytic and antibacterial activities of ZnO thin films prepared by sol-gel dip-coating method, *Adv. Powder Technol.*, 24 (2013) 275–280.
- [37] G. Applerot, N. Perkas, G. Amirian, O. Girshevitz, A. Gedanken, Coating of glass with ZnO via ultrasonic irradiation and a study of its antibacterial properties, *Appl. Surf. Sci.*, 256 (2009) 53–58.
- [38] N.A.K. Aznan, M.R. Johan, Quantum size effect in ZnO nanoparticles via mechanical milling, *J. Nanomater.*, 2012 (2012) 3.
- [39] M.M. Hasan Farooqi, R.K. Srivastava, Enhanced UV-vis photoconductivity and photoluminescence by doping of samarium in ZnO nanostructures synthesized by solid state reaction method, *Optik*, 127 (2016) 3991–3998.
- [40] B.D. Cullity, *Elements of X-Ray Diffraction*, Addison Wesley, USA, 1978.
- [41] D. Theyvaraju, S. Muthukumar, M. Ashokkumar, pH-induced modification on the structural, optical and morphological properties of Zn_{0.94}Ni_{0.04}Mn_{0.02}O nanopowders, *J. Mater. Sci. - Mater. Electron.*, 24 (2013) 5189–5198.
- [42] D. Verma, A.K. Kole, P. Kumbhakar, Red shift of the band-edge photoluminescence emission and effects of annealing and capping agent on structural and optical properties of ZnO nanoparticles, *J. Alloys Compd.*, 625 (2015) 122–130.
- [43] V.D. Mote, Y. Purushotham, B.N. Dole, Williamson-Hall analysis in estimation of lattice strain in nanometer-sized ZnO particles, *J. Theor. Appl. Phys.*, 6 (2012) 2251–2255.
- [44] S. Chakraborty, P. Kumbhakar, Observation of bandgap narrowing effect and photoluminescence emission characteristics of chemically synthesized Co doped ZnO nanosheets, *Indian J. Phys.*, 88 (2014) 251–257.
- [45] G.K. Williamson, W.H. Hall, X-ray line broadening from filed aluminium and wolfram, *Acta Metall.*, 1 (1953) 22–31.
- [46] A.J. Huh, Y.J. Kwon, Nanoantibiotics: a new paradigm for treating infectious diseases using nanomaterials in the antibiotics resistant era, *J. Controlled Release*, 156 (2011) 128–145.
- [47] R.Y. Pelgrift, A.J. Friedman, Nanotechnology as a therapeutic tool to combat microbial resistance, *Adv. Drug Delivery Rev.* 65 (2013) 1803–1815.
- [48] Y. Jiang, L. Zhang, D. Wen, Y. Ding, Role of physical and chemical interactions in the antibacterial behavior of ZnO nanoparticles against *E. coli*, *Mater. Sci. Eng., C*, 69 (2016) 1361–1366.
- [49] G. Applerot, A. Lipovsky, R. Dror, N. Perkas, Y. Nitzan, R. Lubart, A. Gedanken, Enhanced antibacterial activity of nanocrystalline ZnO due to increased ROS-mediated cell injury, *Adv. Funct. Mater.*, 19 (2009) 842–852.
- [50] P. Bommersbach, C. Alemany-Dumont, J.P. Millet, B. Normand, Formation and behaviour study of an environment-friendly corrosion inhibitor by electrochemical methods, *Electrochim. Acta*, 51 (2005) 1076–1084.
- [51] S. Chechirlian, P. Eichner, M. Keddám, H. Takenouti, H. Mazille, A specific aspect of impedance measurements in low conductivity media, *Electrochim. Acta*, 35 (1990) 1125–1131.